Transient Voltage Support Strategy of Grid-forming Medium Voltage Photovoltaic Converter in the LCC-HVDC System

Hong Lu, Xianyong Xiao, *Senior Member*, *IEEE*, *Senior Member*, *CSEE*, Guangfu Tang, *Senior Member*, *IEEE*, *Senior Member*, *CSEE*, Zhiyuan He, *Member*, *IEEE*, *Senior Member*, *CSEE*, Zhiguang Lin, *Member*, *CSEE*, Chong Gao, *Member*, *IEEE*, *Member*, *CSEE*, and Zixuan Zheng, *Member*, *IEEE*

***Abstract*—The participation of photovoltaic (PV) plants in supporting the transient voltage caused by commutation failure in the line-commutated-converter-based high voltage direct current (LCC-HVDC) system is of great significance, as it can enhance the DC transmission ability. However, it is found that the grid-following (GFL) PV converters face the problem of mismatch between reactive power response and transient voltage characteristic when the voltage converts from low voltage to overvoltage, further aggravating the overvoltage amplitude. Thus, this article proposes a transient voltage support strategy based on the grid-forming (GFM) medium voltage PV converter. The proposed strategy takes the advantage of the close equivalent electrical distance between the converter and grid, which can autonomously control the converter terminal voltage through GFM control with adaptive voltage droop coefficient. The simulation results show that the proposed strategy can ensure the output reactive power of the PV converter quickly matches the transient voltage characteristic at different stages, indicating that the proposed strategy can effectively support the transient voltage.**

***Index Terms*—Commutation failure, grid-forming (GFM), photovoltaic (PV) converter, reactive power response, transient voltage.**

I. Introduction

THE line commutated converter (LCC)-based high voltage direct current (HVDC) system is an effective way to transmit large-scale photovoltaic (PV) power [1], [2]. Due to the occurrence of commutation failure in the LCC-HVDC system, the sending AC system face the challenge of transient voltage [3]–[5].

A lot of researchers have carried out studies for eliminating the impact of transient voltage on the grid. Table I lists the differences between recently published articles on this topic to clearly identify research gaps. According to Table I, one common approach is to optimize the control of LCC-HVDC system, including improved firing control [6], fuzzy control [7] improved voltage-dependent current order limiter control [8] and constant reactive power control [9]. Furthermore, some studies proposed novel converter topologies, such as capacitor commutated converter (CCC) [10], enhanced capacitor commutated converter (ECCC) [11] and thyristor-based controllable capacitors converter (TBCCC) [12]. Nevertheless, the adaptability of these methods to different grid conditions is weak, which cannot completely prevent commutation failure. In [13], a controllable-line-commutated converter (CLCC) was proposed, which can prevent the commutation failure by using the full-controlled devices. In addition, the reactive power compensators can also be used for supporting the transient voltage, such as synchronous condenser (SC) [14], static compensator (STATCOM) [15] and static var compensator (SVC) [16]. For example, the Qinghai-Henan $\pm$ 800 kV LCC-HVDC system has installed multiple SCs at the renewable energy sources collection stations and rectifier station. This method can effectively support the transient voltage. However, due to the high cost of SC, it will greatly increase the cost.

Apart from these methods mentioned above, as the proportion of renewable energy resources in the sending AC system increases, there will be a large number of grid-connected converters; thus, it is of great significance to use the fast control characteristics of these converters to participate in transient voltage support [17]. Some methods were proposed in the scenario of wind power transmission through the LCC-HVDC system [18]–[21]. In addition, by optimizing the control parameters of PV converters, the transient voltage support effect can also be improved, such as low/high voltage fault ride-through (FRT) current coefficient, active power recovery coefficient and output voltage reference [22]. However, these methods mainly used grid-following (GFL) control architecture, which cannot quickly adjust the voltage to match the transient voltage characteristics, and may cause small disturbance stability problems in weak grids [23], [24].

Grid-forming (GFM) technology is becoming a highly potential solution to enhance the system stability and grid

Manuscript received January 26, 2024; revised May 1, 2024; accepted June 15, 2024. Date of online publication September 19, 2024; date of current version August 31, 2024. This work was supported by the Science and Technology Project of State Grid Corporation of China (5500-202258115A-1-1-ZN).

H. Lu is with the College of Electrical Engineering, Sichuan University, Chengdu 610065, China, and also with the State Key Lab of Advance Power Transmission Technology, China Electric Power Research Institute, Beijing 100192, China.

X. Y. Xiao (corresponding author, email: xiaoxianyong@163.com) and Z. X. Zheng are with the College of Electrical Engineering, Sichuan University, Chengdu 610065, China.

G. F. Tang, Z. Y. He, Z. G. Lin, and C. Gao are with the State Key Lab of Advance Power Transmission Technology, China Electric Power Research Institute, Beijing 100192, China.

DOI: 10.17775/CSEEJPES.2024.00600

TABLE I
COMPREHENSIVE COMPARISON OF TRANSIENT VOLTAGE SUPPORT METHODS

Type	Reference	Year	Description
Optimizing the control of LCC-HVDC system	[6]	2023	Generate synchronous phases by the voltage of the non-fault phase, and correct the firing control
	[7]	2024	Adjust the rectifier firing angle by identifying the transient voltage stage based on fuzzy clustering
	[8]	2022	An improved voltage-dependent current order limiter control
	[9]	2021	The proposed constant reactive power control can reduce the exchange reactive power between AC and DC systems
Novel converter topologies	[10]	1998	The proposed capacitor commutation converter can improve the commutation margin
	[11]	2018	An evolved capacitor commutation converter with antiparallel thyristors based dual-directional full-bridge is proposed
	[12]	2018	The proposed thyristor-based controllable capacitor connects the thyristor module to increase the commutation voltage
	[13]	2023	The proposed controllable line commutation converter is composed of IGBT and thyristor, and can fundamentally solve the problem of commutation failure
Reactive power compensation equipment	[14]	2019	The impact of synchronous condenser (SC) on mitigating commutation failure is analyzed, indicating that SC can reduce transient overvoltage amplitude
	[15]	2022	The impact of STATCOM on the grid strength is evaluated, indicating that STATCOM can support the voltage
	[16]	2022	The impact of static var compensator (SVC) on voltage stability is analyzed, indicating that SVC can support the voltage, but the response speed is slow
Utilizing the fast control characteristics of grid-connected converters	[18]	2021	An improved continuous fault-ride through strategy
	[19]	2021	A delay compensation control strategy of wind turbine converter
	[20]	2021	High voltage ride through is achieved by controlling the energy and rotor converters
	[21]	2022	A power coordinated control strategy for wind farms
	[22]	2019	A method for correcting the voltage reference of PV converter

supporting ability [25], [26]. Some researchers have studied the FRT strategy of GFM converters to improve the operational performance during low voltage faults [27], [28]. In [29], the transient voltage stability problem of GFM converters was revealed, and a method was proposed to improve the transient voltage stability. With the continuous variation of transient voltage during commutation failure in the LCC-HVDC system, the existing methods that mainly focus on low or high voltage faults cannot be directly applied to the transient voltage support.

Moreover, traditional PV converters have the characteristics of small capacity and long distance from the point-of-common coupling (PCC) through multiple energy conversion links, resulting in weak reactive power support ability and difficulty in collaborative control. Due to the fact that modular multilevel converter (MMC) technology can improve the output voltage and capacity of single converter, it is suitable for large-scale PV grid-connected systems [30].

In light of the above, this article proposes a transient voltage support strategy based on the medium voltage PV converter. Large-scale distributed PV can be connected to the grid through a novel MMC-based grid-connected converter (PV-HMMC), where the PV cells are directly connected to the submodule (SM) capacitors of the PV-HMMC through an isolated DC/DC converter. This article analyzes the characteristics of transient voltage during commutation failure in the LCC-HVDC system, as well as the impact of traditional GFL PV converters on the transient voltage, and clarifies the control target of PV-HMMC. Then, this article proposes a transient voltage support strategy of PV-HMMC based on the GFM control framework.

The main contributions of this article can be concluded as follows:

1) The main reason why traditional GFL-PV converters exacerbate the transient overvoltage amplitude of PV collection station is revealed. The delay in reactive power response caused by control mode switching during commutation failure results in the inability to quickly achieve continuous voltage support.

2) A medium voltage PV converter is proposed to replace traditional PV converters to support the transient voltage. Compared with traditional two-level and three-level PV converters, PV-HMMC has the advantages of larger capacity, higher output voltage level, and closer equivalent electrical distance to the PCC, making it easier to improve the transient voltage support ability of a single converter and reduce the control difficulty of multiple converters.

3) A full process transient voltage support strategy of PV-HMMC based on GFM control framework is proposed, which can achieve spontaneous response and does not require higher-level scheduling instructions. The proposed method solves the problem of mismatch between reactive power response and transient voltage characteristics, thereby effectively supporting the transient voltage. Moreover, a small-signal model of PV-HMMC is established based on impedance method, and system stability is analyzed through Nyquist criterion, which can provide guidance for parameter design.

The rest of this article is organized as follows. Section II illustrates the typical LCC-HVDC system structure and analyzes the transient voltage characteristics of sending AC system during commutation failure. The topology and control strategy design of PV-HMMC are proposed in Section III. Section IV develops a small-signal model of PV-HMMC and analyzed the system stability. The effectiveness of the proposed control strategy is verified by simulation results in Section V. Section VI concludes this article.

II. TRANSIENT VOLTAGE CHARACTERISTICS ANALYSIS OF SENDING AC SYSTEM DURING COMMUTATION FAILURE

In order to analyze the transient voltage characteristics during commutation failure, a system model is built in

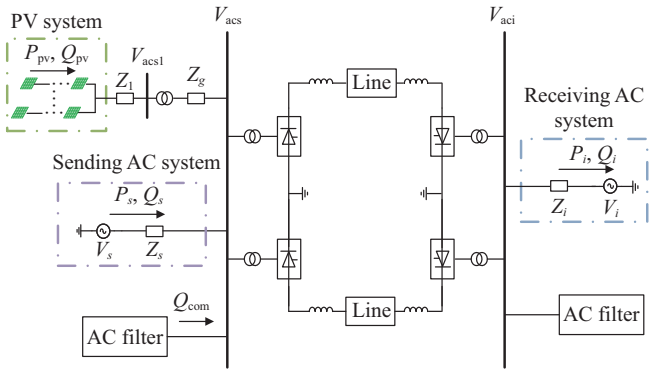

Fig. 1. System topology of large-scale PV transmission through LCC-HVDC.

PSCAD/EMTDC based on the CIGRE benchmark model [31], as shown in Fig. 1. The system parameters are given in Appendix Table AI.

The reactive power consumed by the LCC-HVDC rectifier station can be calculated as [2]:

$$Q_{\mathrm{dc\_r}} = \frac{3N_0}{\pi} I_{\mathrm{dc}} \sqrt{\begin{array}{l} 2T_r^2 V_{\mathrm{acs}}^2 (1-\cos^2\alpha_r) - X_r^2 I_{\mathrm{dc}}^2 \\ +2\sqrt{2} T_r V_{\mathrm{acs}} \cos\alpha_r X_r I_{\mathrm{dc}} \end{array}} \quad (1)$$

where α_r is the firing angle of the rectifier, I_{dc} is the DC current, N_0 is the number of 6-pulse converters, T_r is the transformation ratio of the rectifier transformer, X_r is the connection reactance, and V_{acs} is bus voltage of the sending AC system.

To compare the effects of GFL PV plants on transient overvoltage, two simulation cases have been conducted. Case I: the sending AC system does not contain PV plants. Case II: the sending AC system contains GFL PV plants. The typical configuration of a traditional PV grid-connected system is shown in Fig. 2. Generally, PV converters are controlled by the GFL architecture. In addition, PV converters usually have the FRT ability and can switch to FRT control mode during the grid faults, thereby improving the voltage stability by releasing or absorbing reactive power (Q_{pv}).

In these two cases, commutation failure is simulated by setting a single-phase ground fault in the receiving AC system at $t = 1.2$ s, and the fault duration is 0.05 s. The simulation results are shown in Fig. 3.

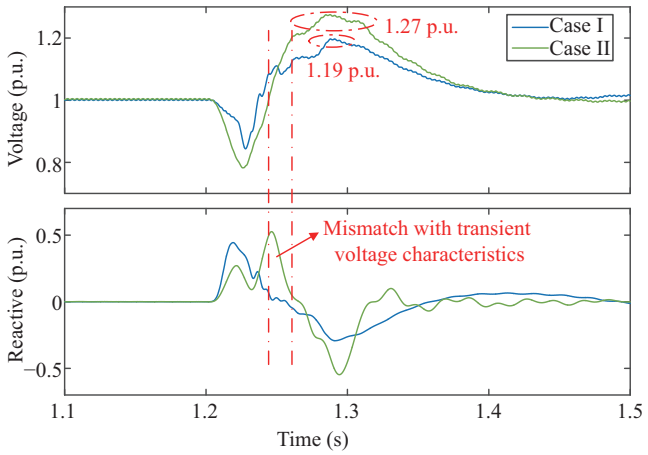

Fig. 3. Transient voltage characteristics during commutation failure.

According to Fig. 3, the reactive power $Q_{\mathrm{dc\_r}}$ increases after a commutation failure occurs, and the rectifier will absorb reactive power from the sending AC system, resulting in V_{acs} decreasing. Then, the DC current gradually decreases to 0 through the DC system control, and the reactive power is injected into the sending AC system, causing V_{acs} to increase to 1.19 p.u.

When large-scale PV plants are connected to the AC bus of the sending AC system, it is necessary to analyze the impact of the control characteristics of the GFL PV converters on transient voltage. As shown in Fig. 3, when the grid voltage drops below the low voltage threshold, the PV converters will switch to the low voltage FRT control mode, supporting the

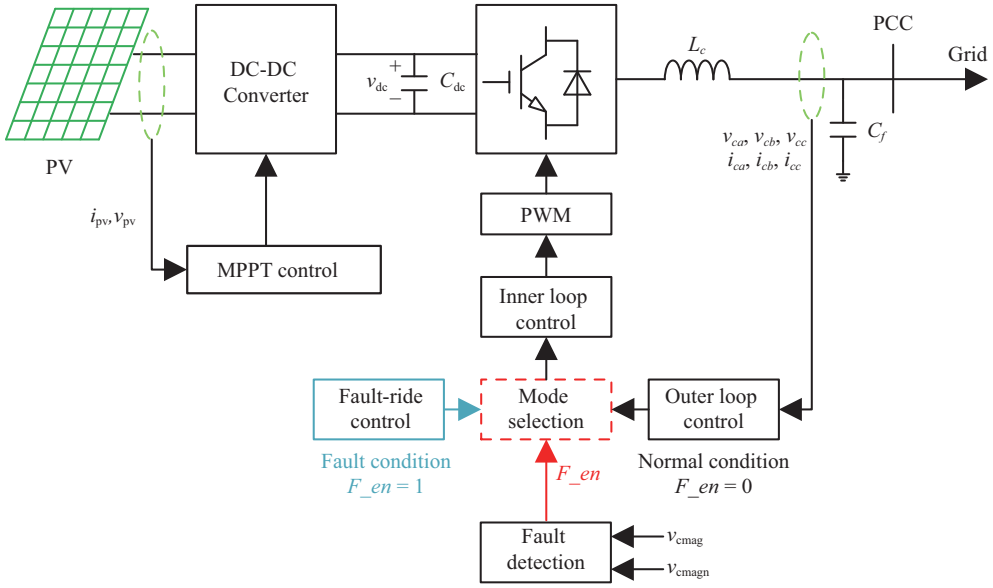

Fig. 2. Circuit and control of a typical GFL PV converter.

grid voltage by reducing active current and increasing reactive current. Since the transient voltage consists of low voltage and overvoltage, when the grid voltage changes from low voltage to overvoltage, the PV converters will experience a certain delay in the output power due to voltage detection and control delay, resulting in the PV converter continuing to providing reactive power during the overvoltage period. Therefore, the reactive power provided by GFL PV converters cannot fully match the transient voltage characteristics, resulting in the overvoltage amplitude of Case II exceeding that of Case I by 0.08 p.u.

In addition, due to the weak overvoltage tolerance of PV converters (1.3 p.u.), when the overvoltage amplitude exceeds 1.3 p.u., it can cause large-scale PV converters to separate from the grid. Furthermore, the overvoltage level will further increase after the separation of PV converters from the grid, posing a risk of cascading failures.

Moreover, when the traditional PV converters adopt GFM control, the voltage control ability can be improved. However, the following problems still exist:

1) The small capacity of a single traditional PV converter results in insufficient adjustable reactive power. In a large-scale PV power plant, the reactive power control response consistency of multiple converters during commutation failure is weak, which increases the difficulty of cooperative control.

2) Traditional PV converters have low output voltages and need to be connected to grid through a transformer, which has a long equivalent electrical distance from grid. Due to the short duration of transient voltage, the control delays result in slow response speed and limited transient voltage support ability.

III. Topology and Transient Voltage Support Control Strategy Design of PV-HMMC

A. Topology of PV-HMMC

PV-HMMC is designed based on MMC technology, as shown in Fig. 4. The main difference is that the DC port of each submodule (PVSM) of PV-HMMC is connected to the PV cells. The topology of the PVSM in PV-HMMC is shown in Fig. 5. PVSM contains PV cells, an active neutral point clamped (ANPC) - dual active bridge (DAB) circuit, a DC-side capacitor and a full-bridge circuit. ANPC-DAB circuit can provide the electrical isolation between the PV cells and grid. Due to the PV cells are mainly connected to the converter through 1500 V DC cable, the primary side of the DAB converter is selected an ANPC circuit, which can reduce the voltage stress of the switches and be applied in the field of large-capacity transmission. In addition, the DC/AC conversion link connected to the MMC-side adopts the full-bridge circuit, which can be beneficial for improving the voltage regulation range and achieving capacitor voltage balance.

According to Fig. 4, the arm voltages can be obtained:

$$\begin{cases} \dfrac{V_{\rm dc}}{2} - v_{\rm uk} - L_{\rm arm}\dfrac{{\rm d}i_{\rm uk}}{{\rm d}t} = L_g\dfrac{{\rm d}i_{\rm ck}}{{\rm d}t} + v_{\rm gk} \\ -\dfrac{V_{\rm dc}}{2} + v_{\rm lk} + L_{\rm arm}\dfrac{{\rm d}i_{\rm lk}}{{\rm d}t} = L_g\dfrac{{\rm d}i_{\rm ck}}{{\rm d}t} + v_{\rm gk} \end{cases} \tag{2}$$

where $V_{\rm dc}$ is the DC voltage, $L_{\rm arm}$ and L_g are arm and grid inductors, respectively, $i_{\rm uk}$ and $i_{\rm lk}$ are the arm currents, $v_{\rm uk}$ and $v_{\rm lk}$ are the arm voltages, $v_{\rm gk}$ is the grid voltage, and $i_{\rm ck}$ is the current injected into the grid.

The circulating current ($i_{\rm cirk}$) flowing between the upper and lower arms of PV-HMMC meets the following equations:

$$\begin{cases} i_{\rm uk} = i_{\rm ck}/2 + i_{\rm cirk} \\ i_{\rm lk} = -i_{\rm ck}/2 + i_{\rm cirk} \end{cases} \tag{3}$$

In addition, the circulating current can be expressed as:

$$i_{\rm cirk} = I_{\rm cirk}^{\rm dc} + I_{\rm cirk}^{\omega}\cos(\omega t + \varphi_k^{\omega}) \tag{4}$$

where $I_{\rm cirk}^{\rm dc}$ is the DC component, $I_{\rm cirk}^{\omega}$ and φ_k^{ω} are the amplitude and phase angle of the fundamental frequency component, respectively, and ω is the angular frequency.

According to (2) and (3), the references of the arm voltages of PV-HMMC can be obtained as:

$$\begin{cases} v_{\rm uk}^{\rm ref} = \dfrac{V_{\rm dc}}{2} - v_{sk}^{\rm ref} - v_{\rm cirk}^{\rm ref} \\ v_{\rm lk}^{\rm ref} = \dfrac{V_{\rm dc}}{2} + v_{sk}^{\rm ref} - v_{\rm cirk}^{\rm ref} \end{cases} \tag{5}$$

where $v_{sk}^{\rm ref}$ and $v_{\rm cirk}^{\rm ref}$ are the internal and circulating voltage references of PV-HMMC, respectively.

$$v_{sk} = (v_{\rm lk} - v_{\rm uk})/2 \tag{6}$$

$$v_{\rm cirk} = [V_{\rm dc} - (v_{\rm uk} + v_{\rm lk})]/2 \tag{7}$$

Thus, by controlling the arm insertion value of the PV-HMMC, the arm voltages can be regulated and thus the output voltage of the PV-HMMC can be controlled. Since the amplitude and phase of the output voltage can be controlled separately, it can meet the needs of releasing and absorbing reactive power during transient voltage.

B. Control Strategy Design of PV-HMMC

The PV cells are connected with the DC-side capacitor of PVSM through the ANPC-DAB circuit, and the PV power will aggregate to the MMC-side. By uniformly controlling the energy on the MMC-side, the total PV power can be transmitted to the grid. Therefore, it is necessary to collaborate with PVSM-side and MMC-side to jointly support the transient voltage. The overall control diagram of PV-HMMC is shown in Fig. 6.

The PV cells are connected to each PVSM, and the ANPC-DAB converter is controlled to achieve the maximum power point tracking (MPPT) performance. The single-phase-shift control is used to control the PVSM output power:

$$d_{ji}^k = [P_{{\rm pvref},ji}^k - P_{{\rm pv},ji}^k + \Delta P_{{\rm pvref},ji}^k]G_d(s) \tag{8}$$

where $G_d(s) = k_{p1} + k_{i1}/s$ is the PI controller, d_{ji}^k is the phase-shift ratio, $P_{{\rm pvref},ji}^k$ is the maximum power obtained by perturbation observation method, $P_{{\rm pv},ji}^k$ is the output power of the PVSM, and $\Delta P_{{\rm pvref},ji}^k$ is the PV power adjustment value during commutation failure.

MMC level control can be divided into energy balance control and GFM control. This article mainly achieves energy balance control through a circulating current suppression

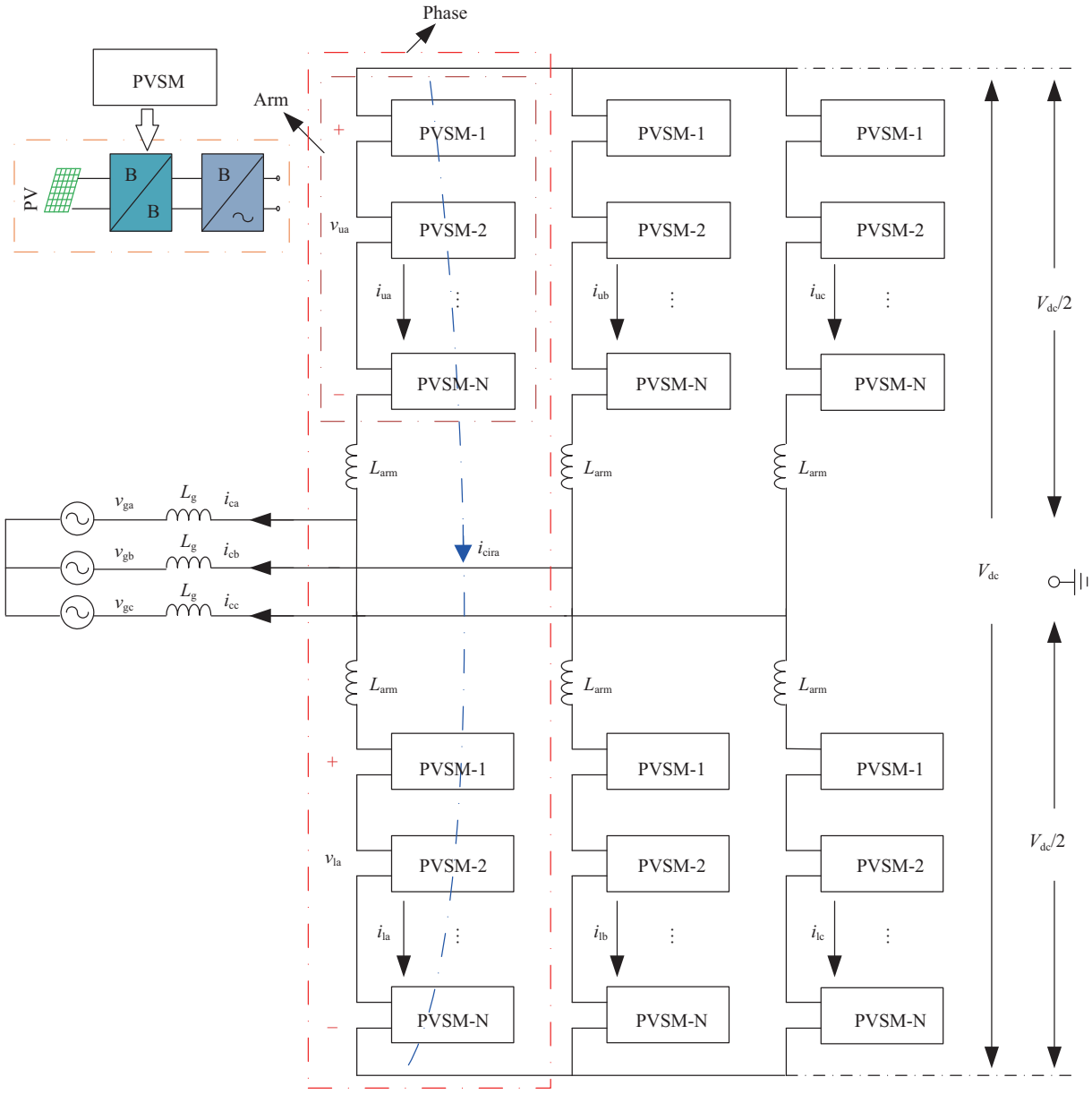

Fig. 4. The structure of PV-HMMC.

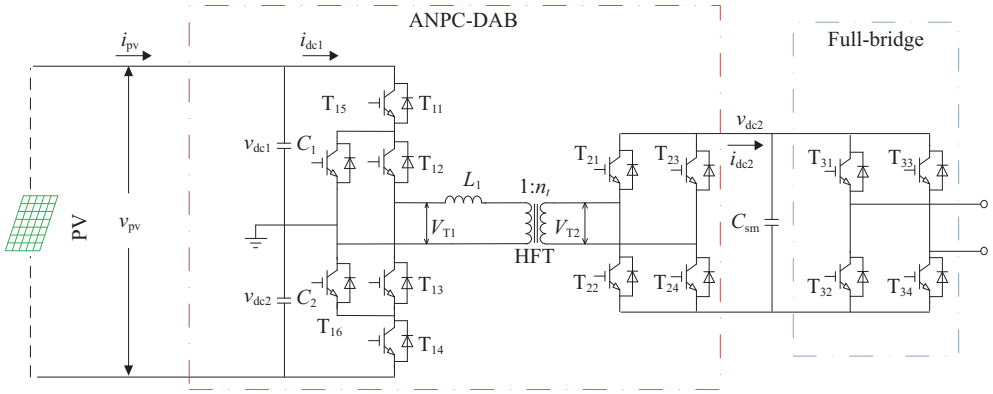

Fig. 5. The PVSM topology of PV-HMMC.

controller (CCSC). According to (4), by controlling the DC and fundamental frequency components of circulating current, the power of each phase and the power of the upper and lower arms in the same phase can be adjusted separately.

Moreover, the energy balance between different PVSMs is achieved through carrier phase shift pulse-width modulation (CPS-PWM). Other improved energy control strategies can also be applied to PV-HMMC.

In order to overcome the delay problem caused by the switching control mode of traditional GFL PV converters during grid faults, this article adopts the GFM architecture to design the control strategy of PV-HMMC, which can ensure that PV-HMMC has the ability of continuously supporting the voltage under normal and fault conditions. The GFM control strategy of PV-HMMC is shown in Fig. 7.

The PVSM capacitor voltage can reflect the power balance between the PV-HMMC and grid. Thus, the phase angle θ_c can be obtained via the following equation:

$$\theta_c = \omega_c / s = [(u_{\text{cave}} - u_{\text{caveref}})/M_u + \omega_n]/s \tag{9}$$

where ω_c is the virtual angular frequency, ω_n is the rated angular frequency, u_{caveref} is the average capacitor voltage reference, and M_u is the control coefficient.

The rapid change of transient voltage from low voltage to

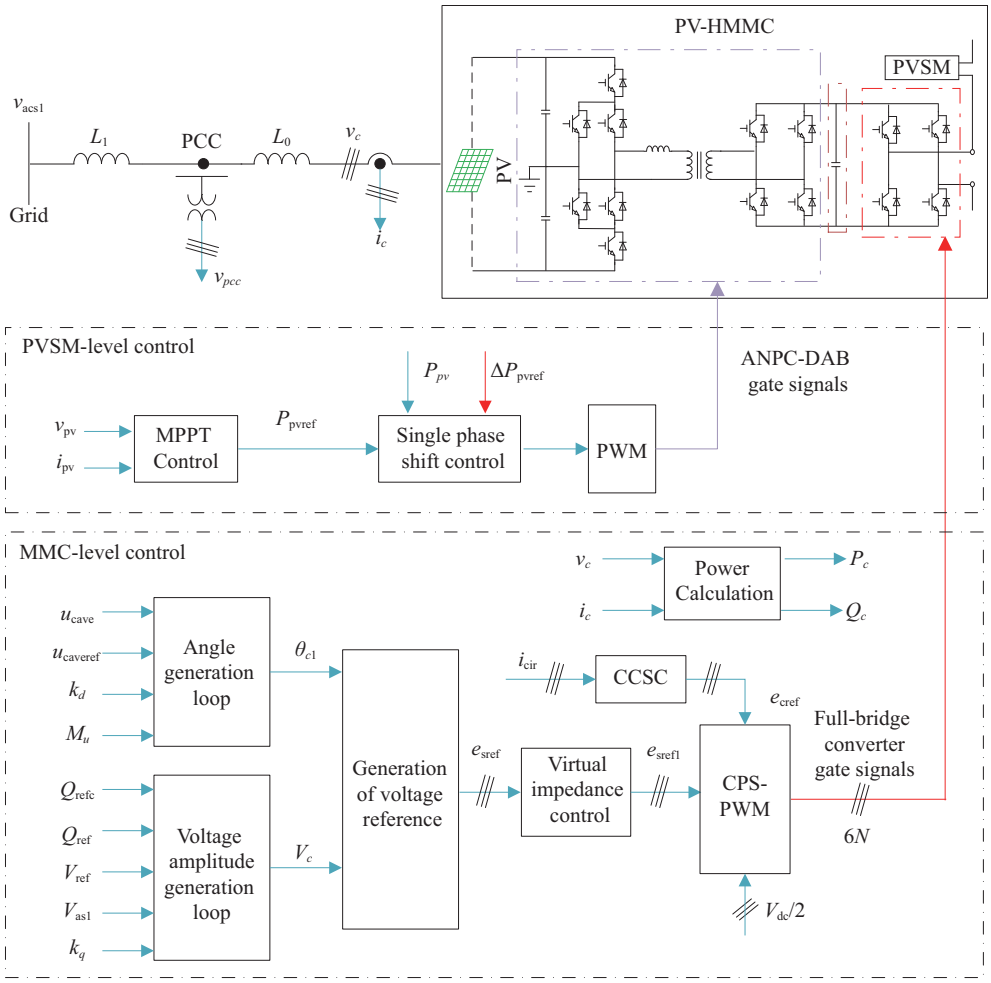

Fig. 6. The overall control diagram of PV-HMMC.

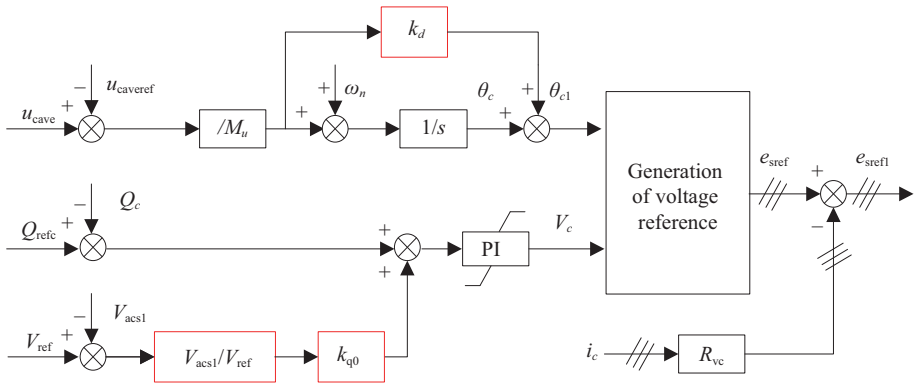

Fig. 7. The GFM control strategy of PV-HMMC.

overvoltage usually occurring within approximately 50 ms, which leads to a sharp change in the output active and reactive power of PV-HMMC. To prevent power oscillation, a phase feedforward method is proposed to adjust the phase, which can be expressed as:

$$\Delta\theta_c = k_d(\omega_c - \omega_n) \tag{10}$$

where k_d represents the damping coefficient.

Then, combining (9) and (10), it yields:

$$\theta_{c1} = \theta_c + \Delta\theta_c \tag{11}$$

For the voltage amplitude generation loop, the control law is given by:

$$V_c = [\Delta Q_{\mathrm{refc}} + Q_{\mathrm{refc}} - Q_c]G_{\mathrm{q}}(s) \tag{12}$$

where Q_{refc} and Q_c are the reference and actual value of the output reactive power of PV-HMMC, respectively, ΔQ_{refc} is the variation of reactive power reference when transient voltage occurs, $G_{\mathrm{q}}(s) = k_{\mathrm{pv}} + k_{iv}/s$ is the PI controller.

Due to the low voltage and high voltage characteristics of the transient voltage, PV-HMMC needs to instantaneously output and absorb reactive power during the low voltage and high voltage stages, respectively. To accelerate the adjustment of reactive power at different stages, the transient voltage information is added into the reactive power reference:

$$\Delta Q_{\mathrm{refc}} = k_{\mathrm{q}}(V_{\mathrm{ref}} - V_{\mathrm{acs1}}) = (k_{\mathrm{q0}}V_{\mathrm{acs1}}/V_{\mathrm{ref}})(V_{\mathrm{ref}} - V_{\mathrm{acs1}}) \tag{13}$$

where k_{q} is the adaptive droop coefficient, V_{ref} and V_{acs1} are the reference and actual value of the 35 kV AC bus, respectively, and k_{q0} is the constant droop coefficient.

According to (12) and (13), it can be seen that when the grid voltage changes from low to high, PV-HMMC quickly responds to voltage changes through a controller with adaptive coefficient, and timely adjusts the reactive power reference, which can effectively avoid the problem of reactive power and voltage mismatch caused by long response time.

To limit the fault current, the virtual impedance (VI) method is used to modify the voltage reference [32]:

$$e_{\mathrm{sref1}} = e_{\mathrm{sref}} - R_{\mathrm{vc}}i_c \tag{14}$$

where R_{vc} is the virtual resistor.

C. Collaborative Control Strategy between Submodules and Converter

PV-HMMC can timely output and absorb reactive power through the proposed control strategy to support low voltage and overvoltage respectively, preventing the mismatch between reactive power response and transient voltage characteristics. Due to the limited capacity of PV-HMMC, the output active power of PV-HMMC should also change synchronously when outputting or absorbing reactive power. Otherwise, the excess PV power will continue to charge the PVSM capacitor, resulting in overvoltage of the capacitor. Thus, collaborative control between submodules and converters is required during transient voltage support. The output active power of each PVSM needs to be adjusted based on the grid state to prevent significant fluctuations in the capacitor voltage of PVSM from exceeding the threshold.

The power adjustment of each PVSM can be expressed as:

$$\Delta P^k_{\mathrm{pvref},ji} = M_{\mathrm{pv}}\Delta\omega_c \tag{15}$$

where M_{pv} is the droop coefficient of PVSM, and $\Delta\omega_c$ represents the perturbation of virtual angular frequency.

By analogy with the dynamic characteristics of synchronous generator, the parameters of PV-HMMC can be expressed as:

$$H_c = 3M_uNC_{\mathrm{sm}}u_{\mathrm{cave0}}\omega_n/S_n \tag{16}$$

$$k_{\mathrm{pc}} = -6NM_{\mathrm{pv}}M_u \tag{17}$$

$$D_c = k_1k_d \tag{18}$$

where H_c is the inertia coefficient. S_n is the rated capacity of the converter, u_{cave0} is the initial average capacitor voltage, C_{sm} is the value of capacitor, k_{pc} and D_c are the droop and damping coefficients, respectively, and k_1 is the synchronization coefficient.

Thus, PV-HMMC can not only support the transient voltage through the collaboration of PVSM-side and MMC-side, but also possess inertia, primary frequency regulation, and damping abilities. It indicates that during the process of PV-HMMC supporting transient voltage, the frequency stability can be improved simultaneously, and the impact of further exacerbating transient overvoltage event caused by frequency fluctuations can be reduced.

IV. Stability Analysis

A. Small-signal Model of PV-HMMC

To fully utilize the support ability of PV-HMMC on transient voltage, it is necessary to ensure that PV-HMMC can operate stably. Thus, the small-signal model of PV-HMMC based on the impedance method is developed.

According to [35], the dynamic of PV cells can be expressed as:

$$i_{\mathrm{pv}} = (-1/R_{\mathrm{mppt}})v_{\mathrm{pv}} \tag{19}$$

where i_{pv} and v_{pv} are the output current and voltage of PV cells, respectively; R_{mppt} is the equivalent resistance of PV cells.

The input current and output power of PVSM are given by:

$$i_{\mathrm{dc1}} = (-1/R_{\mathrm{mppt}} + sC_{\mathrm{eq}})v_{\mathrm{pv}} \tag{20}$$

$$P_{\mathrm{pv}} = i_{\mathrm{dc2}}v_{\mathrm{dc2}} \tag{21}$$

where C_{eq} is the equivalent capacitor, i_{dc2} and v_{dc2} represent the output current and voltage of ANPC-DAB circuit, respectively.

Substituting (19), (20) and (21) into (8), and applying small-signal linearization to the equation, we can obtain:

$$d^p = [-v^p_{\mathrm{pv}}G_v - (I_{\mathrm{dc20}}v^p_{\mathrm{dc2}} + V_{\mathrm{dc20}}i^p_{\mathrm{dc2}})]G_d \tag{22}$$

where the superscript p and subscript 0 represent the small signal perturbation and steady-state value, respectively, and G_v is the PI controller.

Then, the small signal expression of ANPC-DAB circuit can be expressed as [33]:

$$\begin{cases} i_{\mathrm{dc1}}^{p} = G_1 v_{\mathrm{dc2}}^{p} + G_2 d^{p} \\ i_{\mathrm{dc2}}^{p} = G_3 v_{\mathrm{pv}}^{p} + G_4 d^{p} \end{cases} \tag{23}$$

where f is the switching frequency, n_t is the transformer ratio, L_1 is the transformer inductance, and the expression of G_1–G_4 can be found in Appendix (A1).

Furthermore, the admittance of the ANPC-DAB circuit can be obtained:

$$\begin{aligned} Y_{\mathrm{DAB}} &= \frac{i_{\mathrm{dc2}}^{p}}{v_{\mathrm{dc2}}^{p}} \\ &= \frac{(G_3 - G_4 G_d G_v)(G_1 - G_2 G_d I_{\mathrm{dc20}}) - X_1 G_4 G_d I_{\mathrm{dc20}}}{X_1(1 + G_4 G_d V_{\mathrm{dc20}}) + (G_3 - G_4 G_d G_v) G_2 G_d V_{\mathrm{dc20}}} \end{aligned} \tag{24}$$

where $X_1 = G_2 G_d G_v - (1/R_{\mathrm{mppt}} + sC_{\mathrm{eq}})$.

Thus, the admittance of PVSM can be expressed as:

$$Y_{\mathrm{pvsm}} = Y_{\mathrm{DAB}} + sC_{\mathrm{sm}} \tag{25}$$

For the small-signal modeling on the MMC side, the harmonic state space method is used for implementation. According to [35], the frequency domain equations of MMC can be obtained:

$$\begin{cases} \boldsymbol{V}_{\mathrm{kc}}^{p} = \boldsymbol{G}_{11}\boldsymbol{I}_{\mathrm{kc}}^{p} + \boldsymbol{G}_{12}\boldsymbol{I}_{\mathrm{kd}}^{p} + \boldsymbol{Q}_{11}\boldsymbol{M}_{\mathrm{kc}}^{p} + \boldsymbol{Q}_{12}\boldsymbol{M}_{\mathrm{kd}}^{p} \\ \boldsymbol{V}_{\mathrm{kd}}^{p} = \boldsymbol{G}_{12}\boldsymbol{I}_{\mathrm{kc}}^{p} + \boldsymbol{G}_{11}\boldsymbol{I}_{\mathrm{kd}}^{p} + \boldsymbol{Q}_{12}\boldsymbol{M}_{\mathrm{kc}}^{p} + \boldsymbol{Q}_{11}\boldsymbol{M}_{\mathrm{kd}}^{p} \end{cases} \tag{26}$$

$$\begin{cases} \boldsymbol{Z}_{\mathrm{arm}}^{p}\boldsymbol{I}_{\mathrm{kc}}^{p} = \boldsymbol{V}_{\mathrm{dc}}^{p}/2 - \boldsymbol{V}_{\mathrm{kc}}^{p} \\ \boldsymbol{Z}_{\mathrm{arm}}^{p}\boldsymbol{I}_{\mathrm{kd}}^{p} = -\boldsymbol{V}_{\mathrm{kd}}^{p} - \boldsymbol{V}_{sk}^{p} \end{cases} \tag{27}$$

where subscripts c and d represent the common mode and differential mode operators. $\boldsymbol{G}$ and $\boldsymbol{Q}$ are coefficient matrices. $\boldsymbol{Z}_{\mathrm{arm}}^{p}$ and $\boldsymbol{Y}_{c}^{p}$ represent the arm impedance matrix and the PVSM admittance matrix, respectively. The detailed expressions are shown in Appendix (A2)–(A4).

Then, it is necessary to model the controller on the MMC-side. According to (9), the dynamics of synchronization and reactive power controllers can be expressed as follows:

$$\boldsymbol{\theta}_{c}^{p} = \boldsymbol{G}_{\theta}^{p}\boldsymbol{V}_{\mathrm{cave}}^{p} \tag{28}$$

$$\boldsymbol{V}_{\mathrm{refc}}^{p} = -\boldsymbol{G}_{v}^{p}(\boldsymbol{Q}_{c}^{p} + k_{\mathrm{q}}\boldsymbol{V}_{s}^{p}) \tag{29}$$

where $\boldsymbol{\theta}_{c}^{p}$ is the output angle perturbation of PV-HMMC; $\boldsymbol{G}_{\theta}^{p}$ and $\boldsymbol{G}_{v}^{p}$ are the small-signal complex frequency domain matrices in the synchronization and reactive power controllers. The detailed expressions are shown in Appendix (A5)–(A6).

Thus, the differential mode modulation signal perturbation can be expressed as:

$$\boldsymbol{M}_{\mathrm{kd}}^{p} = \boldsymbol{G}_{vs,md}^{p}\boldsymbol{V}_{sk}^{p} + \boldsymbol{G}_{id,md}^{p}\boldsymbol{I}_{\mathrm{kd}}^{p} \tag{30}$$

where $\boldsymbol{G}_{vs,md}^{p}$ and $\boldsymbol{G}_{id,md}^{p}$ are small-signal complex frequency matrices related to grid voltage and current, respectively, and the detailed derivation process is shown in Appendix (A7) – (A9).

Moreover, CCSC and synchronization controller can also cause common mode current perturbation. Thus, the common mode modulation signal perturbation can be obtained as:

$$\boldsymbol{M}_{\mathrm{kc}}^{p} = \boldsymbol{M}_{\mathrm{kcirc}}^{p} + \boldsymbol{M}_{\mathrm{kcvc}}^{p} = \boldsymbol{G}_{\mathrm{ic,mc}}^{p}\boldsymbol{I}_{\mathrm{kc}}^{p} \tag{31}$$

where $\boldsymbol{G}_{\mathrm{ic,mc}}^{p}$ is the small-signal complex frequency matrix, and the detailed expressions are shown in Appendix (A10)–(A12).

Finally, the small-signal model of PV-HMMC can be obtained as:

$$\begin{aligned} \boldsymbol{Y}_{c}^{p} &= \frac{\boldsymbol{I}_{sk}^{p}}{\boldsymbol{V}_{sk}^{p}} \\ &= \frac{2(\boldsymbol{H}_2\boldsymbol{Q}_{12}\boldsymbol{G}_{vs,md}^{p}(\boldsymbol{H}_1)^{-1} - \boldsymbol{E}\boldsymbol{Q}_{11}\boldsymbol{G}_{vs,md}^{p} - \boldsymbol{E})}{\boldsymbol{Z}_{\mathrm{arm}}^{p} + \boldsymbol{E}\boldsymbol{H}_4 - \boldsymbol{H}_2(\boldsymbol{G}_{12} + \boldsymbol{Q}_{12}\boldsymbol{G}_{id,md}^{p})(\boldsymbol{H}_1)^{-1}} \end{aligned} \tag{32}$$

where the expression of $\boldsymbol{H}_1$–$\boldsymbol{H}_4$ can be found in Appendix (A13).

B. Small-signal Model Validation and Stability Analysis

To verify the accuracy of the proposed small-signal modeling method, a simulation model is built in PSCAD/EMTDC, and the positive-sequence voltage perturbation of different frequencies is injected into PV-HMMC. The results are shown in Fig. 8.

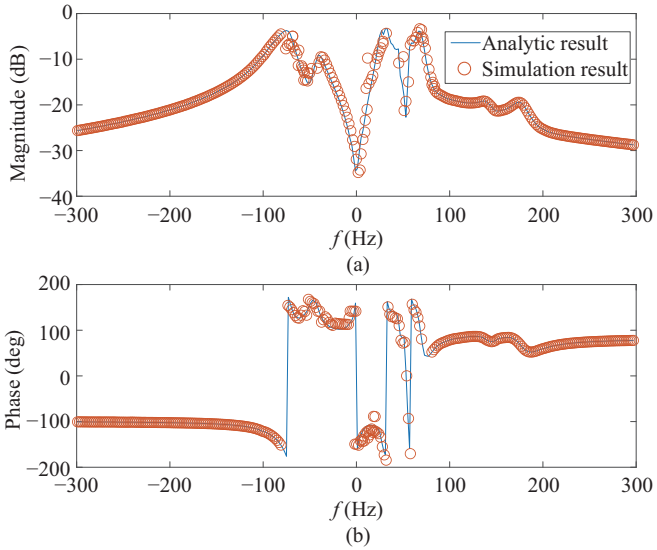

Fig. 8. Analytical and simulation results of the PV-HMMC small-signal model. (a) Magnitude. (b) Phase.

According to Fig. 8, the analytical result and simulation result of the positive-sequence admittance matrix match well, proving the accuracy of the proposed small-signal modeling method of PV-HMMC. Moreover, the Nyquist criterion is further used to analyze the impact of controller parameters on system stability for revealing the stable operation mechanism of PV-HMMC, and the detailed analysis steps can be found in [23]. Taking the synchronization controller as an example, the impacts of different M_u on system stability are analyzed. Other control parameters can be designed based the small-signal model. Fig. 9 shows the generalized Nyquist plots under different M_u. The results show that the system is stable when M_u is 0.1 and 0.4, and the system becomes unstable when M_u is 0.8.

In addition, to verify the accuracy of the stability analysis results based on the small-signal model, the operating characteristics of different M_u are tested in the simulation model,

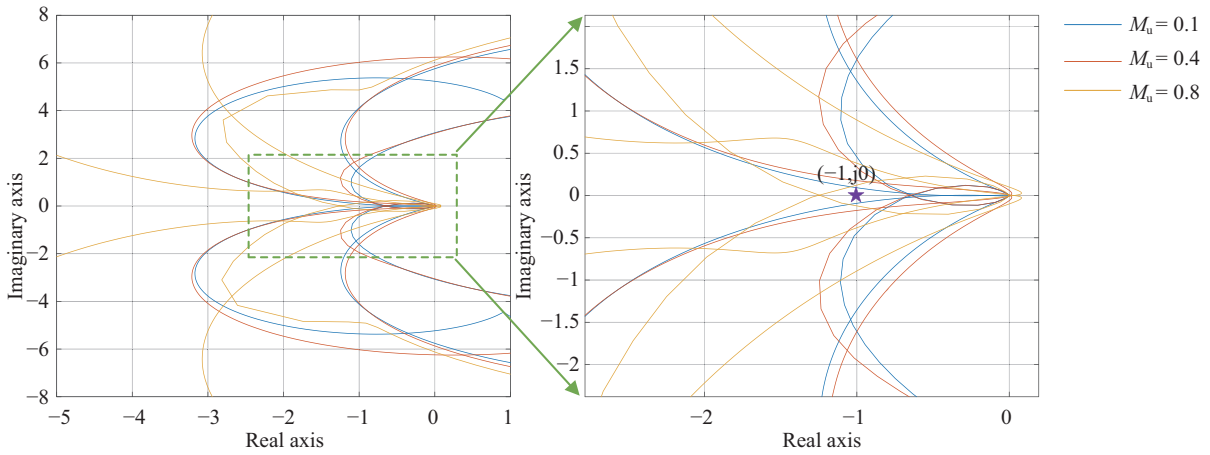

Fig. 9. Generalized Nyquist plots of different M_u.

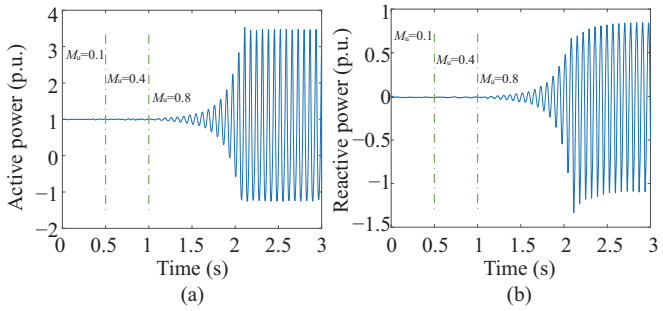

Fig. 10. Simulation results of different M_u. (a) Active power. (b) Reactive power.

and the simulation results are shown in Fig. 10. As shown in Fig. 10, before $t = 1$ s, the system can keep stable. However, after $t = 1$ s, M_u becomes 0.8, and the output power of PV-HMMC oscillates, which is consistent with theoretical analysis and proves the effectiveness of the small-signal model. Thus, in order to ensure system stability and improve the system frequency support ability of PV-HMMC, M_u is selected as 0.4 in this article.

V. Simulation Results

To further verify the effectiveness of the proposed method, the model shown in Fig. 1 is constructed in PSCAD/EMTDC. The proportion of PV power in the sending AC system is 30%, and the main parameters of PV-HMMC are shown in Table II.

A. Transient Voltage Support Performance of PV-HMMC

In order to verify the transient voltage support performance of PV-HMMC, a single-phase ground fault is set in the receiving AC system at $t = 0.2$ s. Fig. 11 shows the simulation results. As shown in Fig. 11(a), both $V_{\rm acs}$ and $V_{\rm acs1}$ exhibit a characteristic of "first decrease then increase" during commutation failure. The transient overvoltage amplitudes of $V_{\rm acs}$ and $V_{\rm acs1}$ are 1.21 p.u. and 1.28 p.u., respectively. During the low voltage stage, PV-HMMC can automatically adjust the reactive power to ensure the stability of the internal voltage, and the maximum output reactive power reaches 0.8 p.u.

TABLE II
Main Circuit Parameters of PV-HMMC

Description	Symbol	Value
Rated capacity	S_{nc}	50 MVA
Rated active power	P_{nc}	45 MW
Rated AC voltage	V_c	35 kV
Number of PVSMs	N	42
Capacitor of PVSM	$C_{\rm sm}$	8500 μF
Arm inductance and resistance	$L_{\rm arm}$, $R_{\rm arm}$	18.7 mH, 1 Ω
Rated grid frequency	f_n	50 Hz
Control parameters of	M_u	0.4
synchronization loop	$k_{\rm dc}$	0.03
Droop coefficient of PVSM	$M_{\rm pv}$	6
Control parameters of reactive	$k_{\rm pv}$, $k_{\rm qv}$	0.4, 0.5
power loop	$k_{\rm q}$	5
Voltage reference	$V_{\rm ref}$	1 p.u.
Average capacitor voltage reference	$u_{\rm caveref}$	1 kV
Reactive power reference	$Q_{\rm refc}$	0 Mvar

During the transition from low to high voltage, PV-HMMC can quickly adjust to the mode of absorbing reactive power.

Figure 11(b) shows the average capacitor voltage and arm voltage. After a fault occurs, PV-HMMC requires sufficient reactive power to support the voltage, resulting in a decrease in the output active power. When the PVSM cannot immediately respond to changes in grid power, the arm voltage will experience small fluctuations, and $u_{\rm cave}$ increases to 1.08 p.u. After the fault is cleared, $u_{\rm cave}$ decreases to support the system power balance and gradually returns to the rated value.

Figure 12 shows the simulation results of PVSMs during commutation failure. In normal operation, each PVSM operates in the MPPT mode, and immediately switches to non-MPPT mode after a fault occurs. Then, the output active power of each PVSM can match the grid demand, effectively preventing $u_{\rm cave}$ from exceeding the maximum deviation value ($\pm$ 1.15 p.u.). Thus, during the continuous change of voltage, the active and reactive power of the PV-HMMC can be adjusted according to the needs of the grid, achieving support for the transient voltage.

B. Effectiveness Analysis of Sending AC Grid With Different Short Circuit Ratio

The strength of the sending AC system has a significant impact on the minimum value ($V_{\rm L,min}$) and maximum value

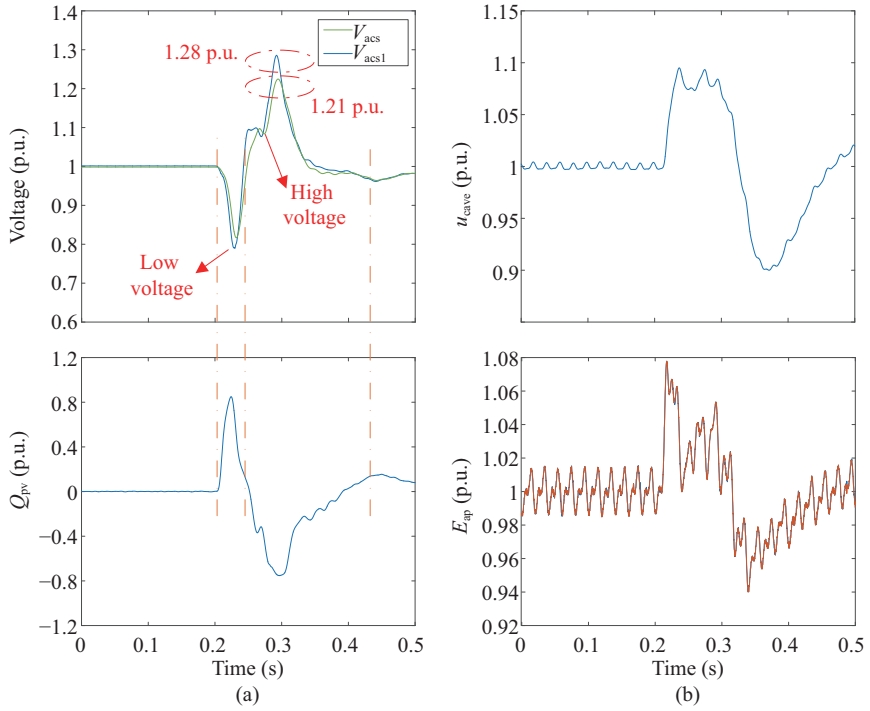

Fig. 11. Simulation results during commutation failure of the proposed method. (a) Transient voltage and reactive power of the PV-HMMC. (b) Average capacitor voltage and arm voltage.

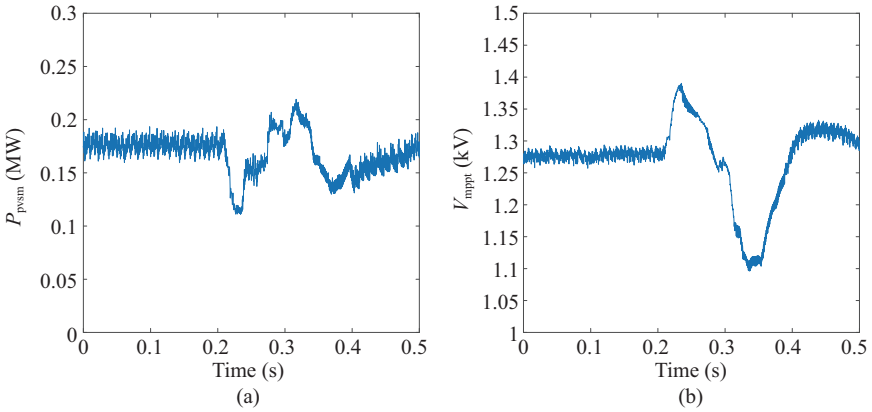

Fig. 12. Signals of PVSMs during commutation failure. (a) Active power provided by each PVSM. (b) Voltage at maximum power operating point.

($V_{\mathrm{H,max}}$) of the transient voltage V_{acs}. Thus, the effectiveness of the proposed strategy under different grid strength is evaluated. The simulation results are shown in Table III.

TABLE III
COMPARISON RESULTS OF THE TRANSIENT VOLTAGE WITH DIFFERENT SCRS

SCR	GFL PV-HMMC		GFM PV-HMMC	
	$V_{\mathrm{L,min}}$	$V_{\mathrm{H,max}}$	$V_{\mathrm{L,min}}$	$V_{\mathrm{H,max}}$
2	0.72 p.u.	1.33 p.u.	0.78 p.u.	1.25 p.u.
2.5	0.79 p.u.	1.29 p.u.	0.82 p.u.	1.21 p.u.
3	0.84 p.u.	1.26 p.u.	0.85 p.u.	1.18 p.u.
5	0.88 p.u.	1.19 p.u.	0.91 p.u.	1.13 p.u.

According to Table III, as SCR decreases from 5 to 2, $V_{\mathrm{L,min}}$ gradually decreases, and $V_{\mathrm{H,max}}$ increases. For GFM PV-HMMC proposed in this article, $V_{\mathrm{L,min}}$ decreases from 0.91 p.u. to 0.78 p.u., and $V_{\mathrm{H,max}}$ increases from 1.13 p.u. to 1.25 p.u. However, the results under the same SCR indicate that the voltage support efficacy of GFL PV-HMMC is weaker than that of GFM PV-HMMC. When the SCR is small, such as SCR $=$ 2, $V_{\mathrm{H,max}}$ reaches 1.33 p.u., which exceeds the voltage tolerance ability of PV-HMMC, resulting in the separation of the converter from grid. Thus, GFM PV-HMMC can effectively support low voltage and overvoltage under different SCR. Moreover, the proposed method has strong adaptability to different SCRs and can support the transient voltage even when SCR is 2.

C. The Impact of Oscillation Damping on Transient Voltage Support Performance

The active and reactive power provided of PV-HMMC will rapidly change during the low and high voltage stages. Fig. 13 shows the simulation results with oscillation damping and

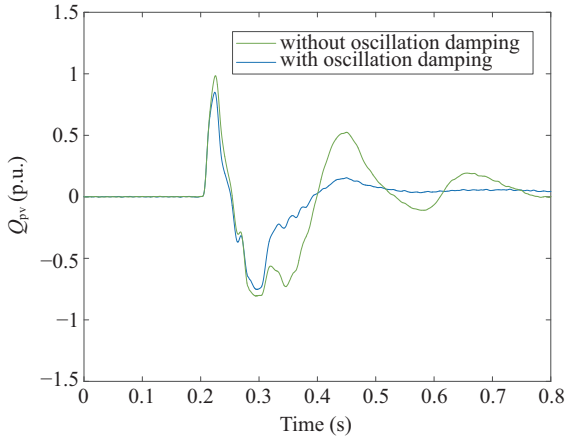

Fig. 13. Simulation results with oscillation damping and without oscillation damping.

without oscillation damping. According to Fig. 13, the reactive power provided by PV-HMMC with oscillation damping exhibits a small overshoot. Moreover, the proposed oscillation damping method helps to reduce settling time, improve the dynamic response speed of PV-HMMC, and achieve effective support for transient voltage.

D. Comparison With Other Methods

The proposed strategy is also compared with the traditional PV grid-connection scheme (two-level PV converter topology) and the improved voltage dependent current order limited (VDCOL) control method proposed in [8]. The simulation results are shown in Fig. 14.

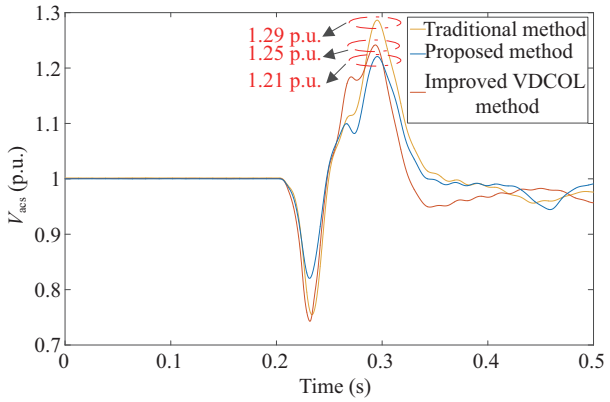

Fig. 14. Simulation results of different control methods.

According to Fig. 14, it can be seen that the transient overvoltage amplitude of the AC bus at the sending system reaches 1.29 p.u. when using the traditional PV grid-connection scheme. After adding the improved VDCOL control method, the transient overvoltage amplitude reduces to 1.25 p.u. However, this method mainly reduces excess reactive power in the sending AC system by optimizing the DC current recovery speed, thereby reducing the transient overvoltage amplitude, and has weak support ability for low voltage and the transient voltage of the PV collection stations. The proposed control strategy can adjust the voltage of PV-HMMC and ensure continuous operation in GFM mode, regardless of whether the voltage is low or high. In addition, the proposed control strategy is unaffected by the fault detection module, and timely absorb reactive power. Thus, the reactive power of PV-HMMC matches the transient voltage characteristics, thereby effectively suppressing the transient overvoltage amplitude.

E. Robustness Analysis of the Proposed Method

1) Different Droop Coefficients

Due to the close equivalent electrical distance between PV-HMMC and grid, the output voltage will be quickly adjusted through the droop controller. Thus, the droop coefficient has a significant impact on the transient voltage support performance. Fig. 15 shows the simulation results of different droop coefficients.

Based on Fig. 15(a), when k_{q0} is small, the range of reactive power reference variation is narrow, and the transient voltage support ability is limited, and there is still a problem of mismatch between reactive power and transient voltage characteristics, resulting in limited support capacity for transient voltage. As k_{q0} increases, the reactive power reference will quickly become negative, thereby achieving suppression of transient overvoltage amplitude. However, when k_{q0} is too large, it will increase the risk that the converter output reactive power is larger than the operation interval due to the large change of the reactive power reference, which leads to the converter overcurrent protection action and threatens the safe and stable operation of the grid. Thus, in this article, k_{q0} is chosen to be 5 to effectively support the transient voltage in the converter reactive power operation interval.

In addition, the effects of adaptive droop coefficient and constant droop coefficient on transient voltage support performance are also compared. It can be seen from Fig. (15) b that the transition from low voltage to high voltage of V_{acs1} results in the value of V_{acs1}/V_{ref} is greater than 1. The use of adaptive droop coefficient in the voltage control loop can ensure that PV-HMMC quickly adjusts the reactive power reference, which is beneficial for improving the response speed to transient high voltage and preventing PV-HMMC from continuing to output reactive power during the high voltage stage. However, due to the short transition time from low voltage to high voltage, if a constant droop coefficient is used to adjust the reactive power reference, it will still result in a delay of about 10 ms in the reactive power response. At this time, the reactive power provided by PV-HMMC cannot match the transient voltage characteristic, resulting in a transient overvoltage amplitude of 1.26 p.u., which is 0.05 p.u. higher than that of adaptive droop coefficient method.

2) PV System Operating Point Change

In normal operating conditions, PV-HMMC can not only provide active power, but also release and absorb reactive power over a large operating range. However, the illumination variations lead to changes in the operating point of PV system and redistribution of active and reactive power in the PV-HMMC. Therefore, the control performance under different illuminations (600 W/m^2, 800 W/m^2, 1000 W/m^2

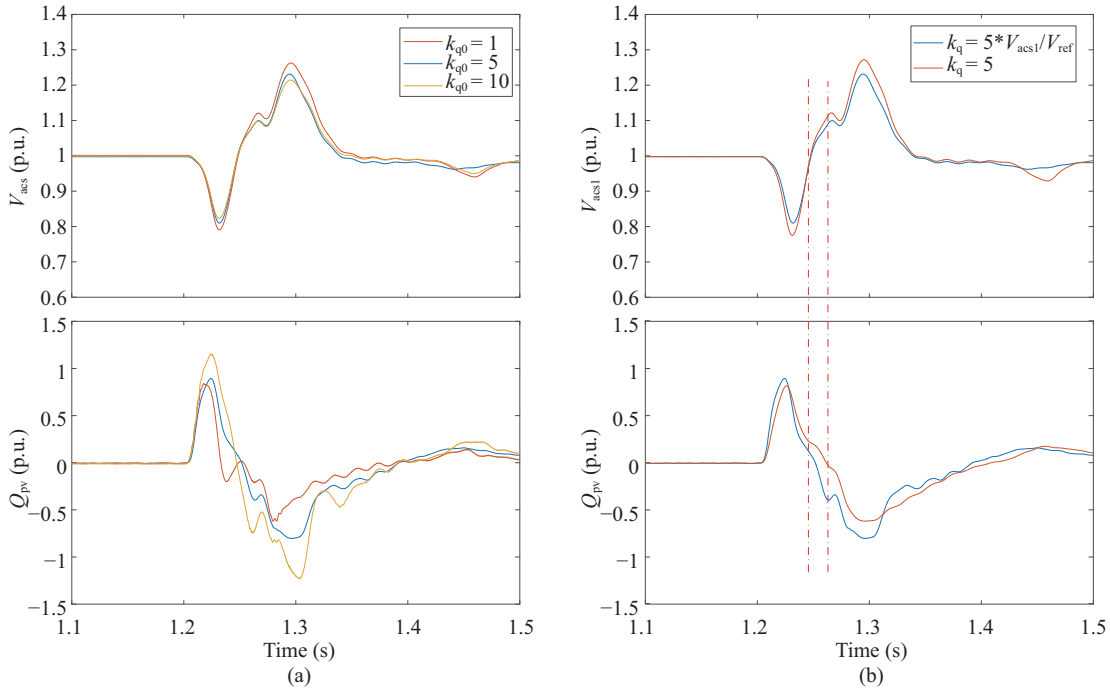

Fig. 15. Simulation results of different droop coefficients. (a) Adaptive droop coefficient. (b) Constant droop coefficient.

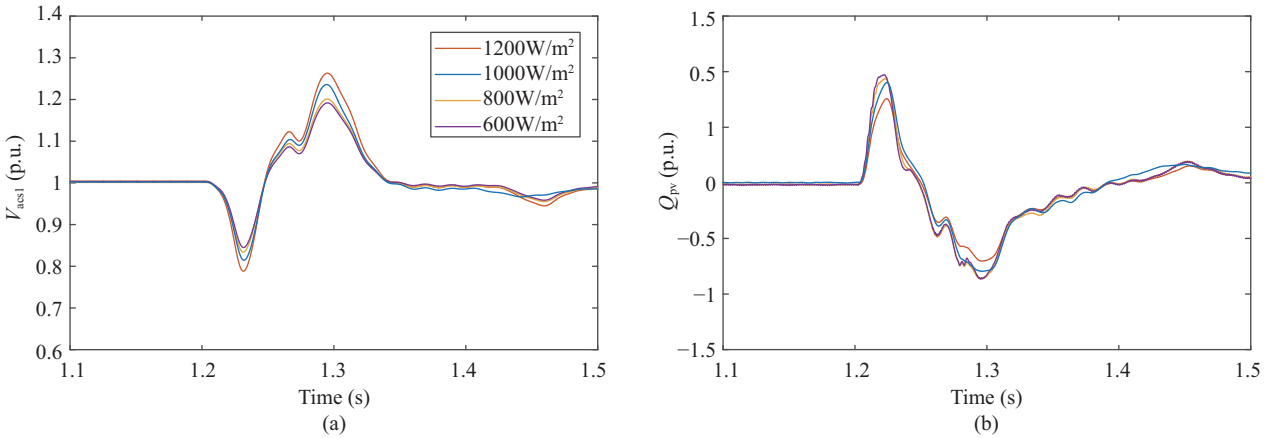

Fig. 16. Simulation results under different illumination. (a) Voltage of the 35 kV AC bus. (b) Reactive power provided by PV plant.

and 1200 W/m^2) is tested. The temperature is set at the rated 25°C in all cases. The simulation results are shown in Fig. 16.

According to Fig. 16, when the illumination decreases, the output active power decreases and the reactive power variation range for transient voltage support will further increase. During commutation failure, the reactive power that can be released and absorbed by the PV-HMMC increases, which is conducive to enhancing the low voltage amplitude and reducing the overvoltage amplitude. It is verified that the illumination will have influence on transient voltage support performance.

3) Voltage Level of PV-HMMC Change

To test the transient voltage support performance at different voltage levels, the comparison is carried out from two cases. Case 1: The output voltage level of PV-HMMC is 35 kV. Case 2: The output voltage level of PV-HMMC is 10 kV, and a step-up transformer (10 kV/ 35 kV) is required. The simulation results are shown in Fig. 17.

According to Fig. 17, when the output voltage of PV-HMMC is 35 kV, it can be directly connected to the grid, thus controlling the converter output voltage to support the transient voltage. However, when the output voltage is 10 kV, it needs to be connected to the grid through a step-up transformer, which reduces the reactive power response speed and leads to the transient overvoltage amplitudes at the PV collection station and the rectifier station to be more than Case 1. Therefore, the reduction of voltage level further reduces the transient voltage support ability of PV-HMMC, which proves the effectiveness of choosing medium voltage as the control target.

4) System Frequency Support Characteristic

To further analyze the impact of PV-HMMC on frequency characteristics of the sending AC system, an equivalent synchronous generator model is used to represent the sending AC system. Furthermore, the proposed method is compared with

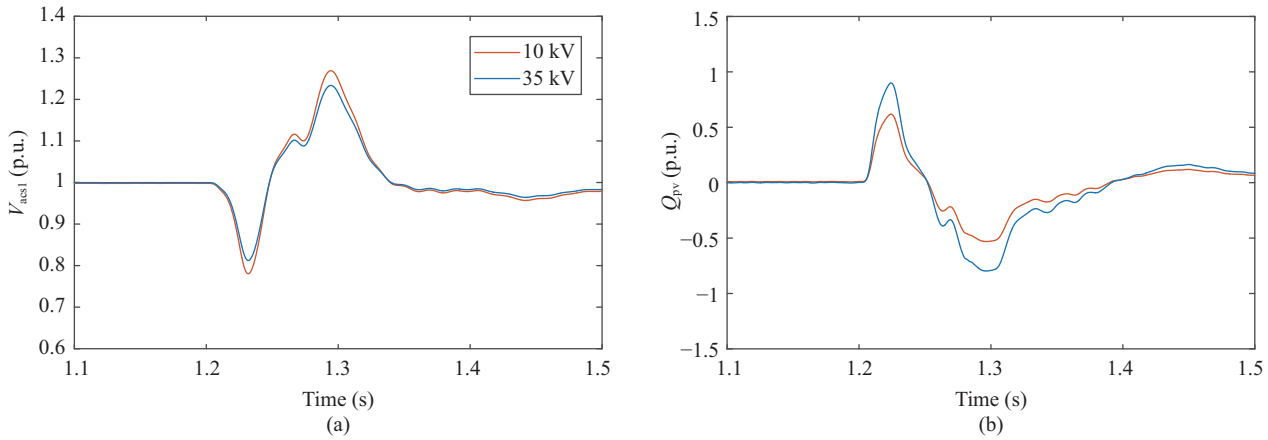

Fig. 17. Simulation results under different voltage levels of PV-HMMC. (a) Voltage of the AC bus. (b) Reactive power provided by PV plant.

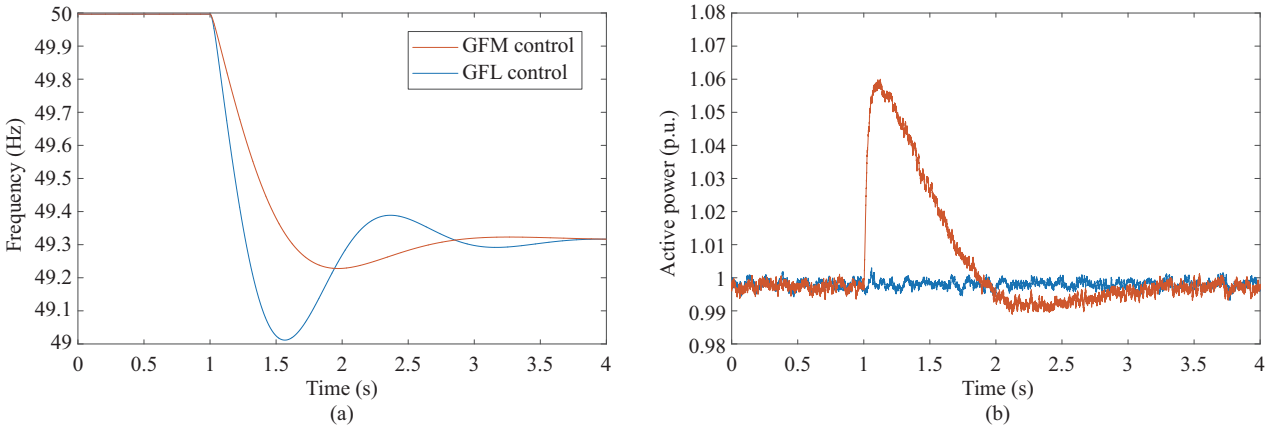

Fig. 18. Simulation results of load increasing condition. (a) Grid frequency. (b) Active power provided by PV-HMMC.

the traditional GFL method using voltage and current dual loop control architecture. By adding a load of 60 MW to the sending AC system, the system power imbalance is simulated. The simulation results are shown in Fig. 18.

According to Fig. 18, it can be seen that at $t = 1$ s, the system load increases, leading to a decrease in the frequency of the sending AC system. Due to the inability of GFL PV-HMMC to respond to system frequency changes, the output power remains unchanged, and the frequency nadir (f_{nadir}) and initial rate of change of frequency (RoCoF) are 49.01 Hz and -0.29 Hz/s, respectively. GFM PV-HMMC has inertia support ability, which can provide inertia power after system frequency changes, thereby increasing f_{nadir} and initial RoCoF to 49.23 Hz and -0.16 Hz/s, respectively. It should be pointed out that this article only studied the scenario of PV-HMMC participating in grid frequency support. The role of DC system and other grid frequency regulation resources can be further considered to achieve grid frequency support, which is of great significance for improving system frequency stability.

VI. Conclusion

To fully utilize the reactive power regulation ability of PV converters, this article has proposed an effective transient voltage support strategy of GFM PV-HMMC during commutation failure in the LCC-HVDC system. The phenomenon of mismatch between reactive power response and transient voltage characteristics caused by traditional GFL PV converters is revealed. By improving the PV converter topology and GFL control, the proposed method achieves continuous operation in GFM mode during commutation failure, ensuring that the provided reactive power matches the transient voltage characteristics. A small signal model of PV-HMMC has been established to analyze the system stability. Based on the simulation results, compared with the GFL PV-HMMC, the reactive power response speed of the proposed method can be further improved, and has strong adaptability to different SCRs of the sending AC system. Compared with traditional PV grid connection method and existing improved DC system control method, the proposed method can regulate the reactive power to quickly match the continuous changes in transient voltage, thereby improving the low voltage and overvoltage support abilities. Furthermore, the impact of illumination, output voltage level and control parameters on transient voltage support performance is analyzed.

For practical application of the proposed method, the author will conduct further research through hardware experiments to validate control efficacy of the proposed method in the actual implementation process.

APPENDIX

$$\begin{aligned} G_1 &= d_0(1-d_0)/2n_t f L_1 \\ G_2 &= V_{\mathrm{dc20}}(1-2d_0)/2n_t f L_1 \\ G_3 &= d_0(1-d_0)/4n_t f L_1 \\ G_4 &= V_{\mathrm{pv0}}(1-2d_0)/4n_t f L_1 \end{aligned} \tag{A1}$$

The relationship between DC voltage perturbation and common mode voltage perturbation can be expressed as:

$$\boldsymbol{V}_{\mathrm{dc}}^{p} = \boldsymbol{G}_{\mathrm{vc,dc}}^{p} \boldsymbol{V}_{\mathrm{kc}}^{p} \tag{A2}$$

TABLE AI
SIMULATION PARAMETERS OF THE LCC-HVDC SYSTEM

Symbol	Parameter	Value
P_{dcn}	Rated power	1000 MW
V_{dcn}	Rated DC voltage	500 kV
I_{dcn}	Rated DC current	1 kA
SCRs	SCR of sending AC system	2.5
SCRr	SCR of receiving AC system	2.5
V_{acsn}	Rated voltage of the sending AC system	345 kV
V_{rn}	Rated voltage of the receiving AC system	230 kV
Q_{comn}	Rated capacity of reactive power compensator	596 Mvar

The expressions for matrices $\boldsymbol{G}$ and $\boldsymbol{Q}$ can be expressed as:

$$\begin{cases} \boldsymbol{G}_{11} = \boldsymbol{M}_{\mathrm{kc0}}(\boldsymbol{Y}_c^p)^{-1}\boldsymbol{M}_{\mathrm{kc0}} + \boldsymbol{M}_{\mathrm{kd0}}(\boldsymbol{Y}_c^p)^{-1}\boldsymbol{M}_{\mathrm{kd0}} \\ \boldsymbol{G}_{12} = \boldsymbol{M}_{\mathrm{kc0}}(\boldsymbol{Y}_c^p)^{-1}\boldsymbol{M}_{\mathrm{kd0}} + \boldsymbol{M}_{\mathrm{kd0}}(\boldsymbol{Y}_c^p)^{-1}\boldsymbol{M}_{\mathrm{kc0}} \\ \boldsymbol{Q}_{11} = \boldsymbol{M}_{\mathrm{kc0}}(\boldsymbol{Y}_c^p)^{-1}\boldsymbol{I}_{\mathrm{kc0}} + \boldsymbol{M}_{\mathrm{kd0}}(\boldsymbol{Y}_c^p)^{-1}\boldsymbol{I}_{\mathrm{kd0}} + \boldsymbol{V}_{\mathrm{kc0}}^{\sum} \\ \boldsymbol{Q}_{12} = \boldsymbol{M}_{\mathrm{kc0}}(\boldsymbol{Y}_c^p)^{-1}\boldsymbol{I}_{\mathrm{kd0}} + \boldsymbol{M}_{\mathrm{kd0}}(\boldsymbol{Y}_c^p)^{-1}\boldsymbol{I}_{\mathrm{kc0}} + \boldsymbol{V}_{\mathrm{kd0}}^{\sum} \end{cases} \tag{A3}$$

where $\boldsymbol{M}_{\mathrm{kc}}$ and $\boldsymbol{M}_{\mathrm{kd}}$ represent the small-signal complex frequency matrixes of common mode modulation signal perturbation and differential mode modulation signal perturbation, respectively. $\boldsymbol{V}_{\mathrm{kc}}$ and $\boldsymbol{V}_{\mathrm{kd}}$ represent the small-signal complex frequency matrixes of common mode arm voltage perturbation and differential mode arm voltage perturbation, respectively.

$$\begin{aligned} \boldsymbol{Z}_{\mathrm{arm}}^{p} &= j2\pi L_{\mathrm{arm}}\,\mathrm{diag}(f_p - nf_n, \cdots, f_p, \cdots, f_p + nf_n) \\ &\quad + \mathrm{diag}(R_{\mathrm{arm}}, \cdots, R_{\mathrm{arm}}, \cdots, R_{\mathrm{arm}}) \\ \boldsymbol{Y}_c^{p} &= \mathrm{diag}\begin{pmatrix} Y_{\mathrm{pvsm}}(j2\pi(f_p - nf_n)), \cdots, Y_{\mathrm{pvsm}}(j2\pi f_p), \\ \cdots, Y_{\mathrm{pvsm}}(j2\pi(f_p + nf_n)) \end{pmatrix} \end{aligned} \tag{A4}$$

where f_p is the perturbation signal, f_n is the rated frequency, and n represents the harmonic order (n is selected as 3).

$$\boldsymbol{G}_{\theta}^{p} = \mathrm{diag}\begin{pmatrix} (1/M_u)(k_d + 1/j2\pi(f_p - nf_n)), \cdots, \\ (1/M_u)(k_d + 1/j2\pi f_p), \cdots, \\ (1/M_u)(k_d + 1/j2\pi(f_p + nf_n)) \end{pmatrix} \tag{A5}$$

$$\boldsymbol{G}_{v}^{p} = \mathrm{diag}\begin{pmatrix} k_{\mathrm{pv}} + k_{iv}/j2\pi(f_p - nf_n), \cdots, \\ k_{\mathrm{pv}} + k_{iv}/j2\pi(f_p), \cdots, \\ k_{\mathrm{pv}} + k_{iv}/j2\pi(f_p + nf_n) \end{pmatrix} \tag{A6}$$

Due to the influence of synchronization controller, reactive power controller, and virtual impedance controllers on common mode modulation signal, the common mode modulation signal perturbation can be represented as:

$$\begin{aligned} \boldsymbol{M}_{\mathrm{kd}}^{p} &= (\boldsymbol{G}_{\mathrm{v,md}}^{p} + \boldsymbol{G}_{\mathrm{vcv,md}}^{p})\boldsymbol{V}_{sk}^{p} \\ &\quad + (\boldsymbol{G}_{\mathrm{i,md}}^{p} + \boldsymbol{G}_{\mathrm{icv,md}}^{p} + \boldsymbol{G}_{\mathrm{ivi,md}}^{p})\boldsymbol{V}_{sk}^{p} \end{aligned} \tag{A7}$$

where $\boldsymbol{G}_{\mathrm{v,md}}^{p}$ and $\boldsymbol{G}_{\mathrm{i,md}}^{p}$ are the small-signal complex frequency domain matrices of reactive power controller, and the detailed expressions can be found in [36]. $\boldsymbol{G}_{\mathrm{vcv,md}}^{p}$ and $\boldsymbol{G}_{\mathrm{icv,md}}^{p}$ are the small-signal complex frequency domain matrices of the synchronization controller. $\boldsymbol{G}_{\mathrm{ivi,md}}^{p}$ is the small-signal complex frequency domain matric of VI controller, $\boldsymbol{G}_{\mathrm{ivi,md}}^{p}(2,2) = \boldsymbol{G}_{\mathrm{ivi,md}}^{p}(4,4) = 2R_{\mathrm{vc}}/V_{\mathrm{dcN}}$.

$$\boldsymbol{G}_{\mathrm{vcv,md}}^{p} = \boldsymbol{G}_{\theta}^{p}\frac{(\boldsymbol{I}_{\mathrm{kc0}} + \boldsymbol{I}_{\mathrm{kd0}})\boldsymbol{G}_{\mathrm{v,md}}^{p}(\boldsymbol{Y}_c^{p})^{-1}}{\boldsymbol{E} - (\boldsymbol{I}_{\mathrm{kc0}} + \boldsymbol{I}_{\mathrm{kd0}})\boldsymbol{G}_{\mathrm{cv},\theta}^{p}(\boldsymbol{Y}_c^{p})^{-1}} \tag{A8}$$

$$\boldsymbol{G}_{\mathrm{icv,md}}^{p} = \boldsymbol{G}_{\theta}^{p}\frac{[(\mathrm{M}_{\mathrm{kc0}} + \boldsymbol{M}_{\mathrm{kd0}}) + (\boldsymbol{I}_{\mathrm{kc0}} + \boldsymbol{I}_{\mathrm{kd0}})\boldsymbol{G}_{\mathrm{i,md}}^{p}](\boldsymbol{Y}_c^{p})^{-1}}{\boldsymbol{E} - (\boldsymbol{I}_{\mathrm{kc0}} + \boldsymbol{I}_{\mathrm{kd0}})\boldsymbol{G}_{\mathrm{cv}\theta}^{p}(\boldsymbol{Y}_c^{p})^{-1}} \tag{A9}$$

where $\boldsymbol{E}$ represents the identity matrix.

The common mode current signal perturbation caused by CCSC and synchronization controller can be expressed as:

$$\boldsymbol{M}_{\mathrm{kcirc}}^{p} = \boldsymbol{G}_{\mathrm{icir,mc}}^{p}\boldsymbol{I}_{\mathrm{kc}}^{p} \tag{A10}$$

$$\boldsymbol{M}_{\mathrm{kcvc}}^{p} = \boldsymbol{G}_{\mathrm{icv,mc}}^{p}\boldsymbol{I}_{\mathrm{kc}}^{p} \tag{A11}$$

where $\boldsymbol{G}_{\mathrm{icir,mc}}^{p}$ and $\boldsymbol{G}_{\mathrm{icv,mc}}^{p}$ are the small-signal complex frequency matrixes of CCSC and synchronization controller, $\boldsymbol{G}_{\mathrm{icir,md}}^{p}(1,1) = \boldsymbol{G}_{\mathrm{icir,md}}^{p}(5,5) = [k_{\mathrm{pc}} + k_{\mathrm{ic}}/j2\pi(f_p - f_n)]/V_{\mathrm{dcN}}$.

$$\begin{aligned} &\boldsymbol{G}_{\mathrm{icv,mc}}^{p} \\ &= \boldsymbol{G}_{\theta}^{p}\frac{(\boldsymbol{M}_{\mathrm{kc0}} + \boldsymbol{M}_{\mathrm{kd0}} + (\boldsymbol{I}_{\mathrm{kc0}} + \boldsymbol{I}_{\mathrm{kd0}})\boldsymbol{G}_{\mathrm{icir,mc}}^{p})(\boldsymbol{Y}_c^{p})^{-1}}{\boldsymbol{E} - (\boldsymbol{I}_{\mathrm{kc0}} + \boldsymbol{I}_{\mathrm{kd0}})\boldsymbol{G}_{\mathrm{cv}\theta}^{p}(\boldsymbol{Y}_c^{p})^{-1}} \end{aligned} \tag{A12}$$

$$\begin{cases} \boldsymbol{H}_1 = 0.5\boldsymbol{E}\boldsymbol{G}_{\mathrm{vc,dc}}^{p} - (\boldsymbol{Z}_{\mathrm{arm}}^{p} + \boldsymbol{G}_{11} + \boldsymbol{Q}_{11}\boldsymbol{G}_{\mathrm{ic,mc}}^{p} \\ \qquad + \boldsymbol{Q}_{12}\boldsymbol{G}_{\mathrm{ic,mc}}^{p})\boldsymbol{H}_3 \\ \boldsymbol{H}_2 = -\boldsymbol{E}(\boldsymbol{G}_{12} + \boldsymbol{Q}_{11}\boldsymbol{G}_{\mathrm{ic,mc}}^{p} + \boldsymbol{Q}_{12}\boldsymbol{G}_{\mathrm{ic,mc}}^{p})\boldsymbol{H}_3 \\ \boldsymbol{H}_3 = (\boldsymbol{Z}_{\mathrm{arm}}^{p})^{-1}(0.5\boldsymbol{G}_{\mathrm{vc,dc}}^{p} - \boldsymbol{E}) \\ \boldsymbol{H}_4 = (\boldsymbol{G}_{11} + \boldsymbol{Q}_{11}\boldsymbol{G}_{id,md}^{p}) \end{cases} \tag{A13}$$

REFERENCES

[1] IEA-PVPS, "Snapshot 2022," IEA-PVPS, 2023.

[2] Q. Xie, Z. X. Zheng, Y. Wang, W. X. Hu, X. Y. Xiao, K. J. Du, and J. Ren, "Analysis of transient voltage disturbances in LCC-HVDC sending systems caused by commutation failures," *IEEE Transactions on Power Delivery*, vol. 37, no. 5, pp. 4370–4381, Oct. 2022.

[3] J. Lu, X. M. Yuan, M. Q. Zhang, and J. B. Hu, "Supplementary control for mitigation of successive commutation failures considering the influence of PLL dynamics in LCC-HVDC systems," *CSEE Journal of Power and Energy Systems*, vol. 8, no. 3, pp. 872–879, May 2022.

[4] Y. H. Lin, B. Wang, Q. L. Guo, H. C. Ge, H. T. Zhao, Y. Z. Zhou, and H. B. Sun, "Volt-VAR secure operational range assessment for preventing initial commutation failures of multi-infeed HVDCs," *CSEE Journal of Power and Energy Systems*, doi: 10.17775/CSEEJPES.2022.05750.

[5] H. Lu, Y. L. Liu, Y. J. Yuan, W. H. Deng, P. F. Su, and X. R. Jiang, "A transient voltage support strategy based on medium voltage photovoltaic grid-connected converter during commutation failure in the LCC-HVDC system," in *Proceedings of the 8th International Conference on Power and Renewable Energy (ICPRE)*, Shanghai, China, 2023, pp. 1658–1664.

[6] Z. X. Yu, J. J. Wang, Y. K. Liu, C. Fu, Q. H. He, Q. M. Wu, and Z. X. Wen, "An improved synchronous firing control on suppressing LCC-HVDC commutation failures caused by single-phase-grounding faults," *IEEE Transactions on Power Delivery*, vol. 38, no. 6, pp. 3875–3887, Dec. 2023.

[7] C. Y. Guo, Q. Ye, X. Y. Chen, and C. Y. Zhao, "Subsequent commutation failure suppression control for LCC-HVDC system based on fuzzy clustering," *CSEE Journal of Power and Energy Systems*, doi: 10.17775/CSEEJPES.2022.05740.

[8] T. Wang, L. Pei, J. M. Wang, and Z. P. Wang, "Overvoltage suppression under commutation failure based on improved voltage-dependent current order limiter control strategy," *IEEE Transactions on Industry Applications*, vol. 58, no. 4, pp. 4914–4922, Jul./Aug. 2022.

[9] C. Y. Yin and F. T. Li, "Reactive power control strategy for inhibiting transient overvoltage caused by commutation failure," *IEEE Transactions on Power Systems*, vol. 36, no. 5, pp. 4764–4777, Sep. 2021.

[10] K. Sadek, M. Pereira, D.P. Brandt, A.M. Gole, and A. Daneshpooy, "Capacitor commutated converter circuit configurations for DC transmission," *IEEE Transactions on Power Delivery*, vol. 13, no. 4, pp. 1257–1264, Oct. 1998.

[11] C. Y. Guo, Z. Z. Yang, B. S. Jiang, and C. Y. Zhao, "An evolved capacitor-commutated converter embedded with antiparallel thyristors based dual-directional full-bridge module," *IEEE Transactions on Power Delivery*, vol. 33, no. 2, pp. 928–937, Apr. 2018.

[12] Y. Xue, X. P. Zhang, and C. H. Yang, "Commutation failure elimination of LCC HVDC systems using thyristor-based controllable capacitors," *IEEE Transactions on Power Delivery*, vol. 33, no. 3, pp. 1448–1458, Jun. 2018.

[13] C. Gao, J. Yang, Z. Y. He, G. F. Tang, J. J. Zhang, T. T. Li, and D. S. He, "Novel controllable-line-commutated converter for eliminating commutation failures of LCC-HVDC system," *IEEE Transactions on Power Delivery*, vol. 38, no. 1, pp. 255–267, Feb. 2023.

[14] A. Aamir, L. Qiao, C. Y. Guo, A. U. Rehman, and Z. Z. Yang, "Impact of synchronous condenser on the dynamic behavior of LCC-based UHVDC system hierarchically connected to AC system," *CSEE Journal of Power and Energy Systems*, vol. 5, no. 2, pp. 190–198, Jun. 2019.

[15] Y. Zhang and A. M. Gole, "Quantifying the contribution of dynamic reactive power compensators on system strength at LCC-HVdc converter terminals," *IEEE Transactions on Power Delivery*, vol. 37, no. 1, pp. 449–457, Feb. 2022.

[16] J. Burr, S. Finney, and C. Booth, "Comparison of different technologies for improving commutation failure immunity index for LCC HVDC in weak AC systems," in *Proceedings of the 11th IET International Conference on AC and DC Power Transmission*, Birmingham, 2015, pp. 1–7.

[17] Z. X. Zheng, J. Ren, X. Y. Xiao, C. J. Huang, Y. Wang, and Q. Xie, "Response mechanism of DFIG to transient voltage disturbance under commutation failure of LCC-HVDC system," *IEEE Transactions on Power Delivery*, vol. 35, no. 6, pp. 2972–2979, Dec. 2020.

[18] T. Zhang, J. Yao, P. Sun, J. X. Pei, H. L. Zhang, K. Liu, and Y. Zhao, "Improved continuous fault ride through control strategy of DFIG-based wind turbine during commutation failure in the LCC-HVDC transmission system," *IEEE Transactions on Power Electronics*, vol. 36, no. 1, pp. 459–473, Jan. 2021.

[19] X. Jin and H. Nian, "Overvoltage suppression strategy for sending AC grid with high penetration of wind power in the LCC-HVDC system under commutation failure," *IEEE Transactions on Power Electronics*, vol. 36, no. 9, pp. 10265–10277, Sep. 2021.

[20] Q. Xie, Z. X. Zheng, X. Y. Xiao, C. J. Huang, J. Q. Zheng, and J. Ren, "Enhancing HVRT capability of DFIG-based wind farms using cooperative rotor-side SMES considering the blocking fault of LCC-HVDC system," *CSEE Journal of Power and Energy Systems*, vol. 7, no. 4, pp. 698–707, Jul. 2021.

[21] X. Jin, H. Nian, C. Zhao, and B. Pang, "Optimal power coordinated control strategy for DFIG-based wind farm to increase transmission capacity of the LCC-HVDC system considering commutation failure," *IEEE Journal of Emerging and Selected Topics in Power Electronics*, vol. 10, no. 3, pp. 3129–3139, Jun. 2022.

[22] B. L. Lou, L. F. Wang, R. Zhang, W. Hua, and J. B. Hu, "Emergency control strategy of PV for suppressing transient overvoltage peak in LCC-HVDC infeed power system," in *Proceedings of the 8th Renewable Power Generation Conference (RPG 2019)*, Shanghai, China, Oct. 2019, pp. 1–6.

[23] K. Ji, G. F. Tang, H. Pang, and J. Yang, "Impedance modeling and analysis of MMC-HVDC for offshore wind farm integration," *IEEE Transactions on Power Delivery*, vol. 35, no. 3, pp. 1488–1501, Jun. 2020.

[24] K. Ji, "Harmonic power modeling for converter-driven stability study," *IEEE Transactions on Power Delivery*, vol. 38, no. 6, pp. 3968–3979, Dec. 2023.

[25] L. D. Zhang, L. Harnefors, and H. P. Nee, "Power-synchronization control of grid-connected voltage-source converters," *IEEE Transactions on Power Systems*, vol. 25, no. 2, pp. 809–820, May 2010.

[26] R. Rosso, X. F. Wang, M. Liserre, X. N. Lu, and S. Engelken, "Grid-forming converters: control approaches, grid-synchronization, and future trends—a review," *IEEE Open Journal of Industry Applications*, vol. 2, pp. 93–109, Apr. 2021.

[27] S. F. Zarei, H. Mokhtari, M. A. Ghasemi, and F. Blaabjerg, "Reinforcing fault ride through capability of grid forming voltage source converters using an enhanced voltage control scheme," *IEEE Transactions on Power Delivery*, vol. 34, no. 5, pp. 1827–1842, Oct. 2019.

[28] B. Fan and X. F. Wang, "Fault recovery analysis of grid-forming inverters with priority-based current limiters," *IEEE Transactions on Power Systems*, vol. 38, no. 6, pp. 5102–5112, Nov. 2023.

[29] J. Y. Fang, W. J. Si, L. T. Xing, and S. M. Goetz, "Analysis and improvement of transient voltage stability for grid-forming converters," *IEEE Transactions on Industrial Electronics*, vol. 71, no. 7, pp. 7230–7240, Jul. 2024.

[30] A. I. Elsanabary, G. Konstantinou, S. Mekhilef, C. D. Townsend, M. Seyedmahmoudian, and A. Stojcevski, "Medium voltage large-scale grid-connected photovoltaic systems using cascaded h-bridge and modular multilevel converters: a review," *IEEE Access*, vol. 8, pp. 223686–223699, Dec. 2020.

[31] M. O. Faruque, Y. Y. Zhang, and V. Dinavahi, "Detailed modeling of CIGRE HVDC benchmark system using PSCAD/EMTDC and PSB/SIMULINK," *IEEE Transactions on Power Delivery*, vol. 21, no. 1, pp. 378–387, Jan. 2006.

[32] T. Liu, X. F. Wang, F. C. Liu, K. Xin, and Y. F. Liu, "A current limiting method for single-loop voltage-magnitude controlled grid-forming converters during symmetrical faults," *IEEE Transactions on Power Electronics*, vol. 37, no. 4, pp. 4751–4763, Apr. 2022.

[33] D. C. Huynh and M. W. Dunnigan, "Development and comparison of an improved incremental conductance algorithm for tracking the MPP of a solar PV panel," *IEEE Transactions on Sustainable Energy*, vol. 7, no. 4, pp. 1421–1429, Oct. 2016.

[34] Y. Eto, Y. Noge, M. Shoyama, and T. Babasaki, "Stability analysis of bidirectional dual active bridge converter with input and output LC filters applying power-feedback control," *IEEE Transactions on Power Electronics*, vol. 38, no. 3, pp. 3127–3139, Mar. 2023.

[35] J. Lyu, X. Zhang, X. Cai, and M. Molinas, "Harmonic state-space based small-signal impedance modeling of a modular multilevel converter with consideration of internal harmonic dynamics," *IEEE Transactions on Power Electronics*, vol. 34, no. 3, pp. 2134–2148, Mar. 2019.

[36] R. C. Pan, G. F. Tang, S. Liu, and Z. Y. He, "Impedance analysis of grid forming control based modular multilevel converters," *Journal of Modern Power Systems and Clean Energy*, vol. 11, no. 3, pp. 967–979, May 2023.

Hong Lu received an M.S. degree in Electrical Engineering from Sichuan University, Chengdu, China, in 2020. He is currently working toward the Ph.D. degree in the College of Electrical Engineering, Sichuan University, Chengdu, China. His current research interests include photovoltaic converter topology, grid-forming control, frequency support and stability analysis.

Xianyong Xiao received the Ph.D. degree from Sichuan University, Chengdu, China, in 2010. He is currently a Professor and the Dean with the College of Electrical Engineering, Sichuan University. His research interests include power quality and its control, distribution system reliability, and green-friendly smart grids.

Guangfu Tang received the B.Eng. degree in Electrical Engineering from Xi'an Jiao Tong University, Xi'an, China, in 1990, and M.Eng. and Ph.D. degrees in Electrical Engineering from the Institute of Plasma Physics, Chinese Academy of Sciences, Hefei, China, in 1993 and 1996, respectively. During 1996–1998, he had a Post-doctoral position with China Electric Power Research Institute (CEPRI), Beijing, China, and he was the Vice-Director of China Energy Conservation Center, Beijing, China. In 1998, he joined CEPRI as an employee, where he led the Thyristor Controlled Series Compensator Group from 1998 to 1999, and the Static Var Compensator Group from 2000 to 2001. Since 2002, he has been a Professor-level Senior Engineer with CEPRI. In 2012, he joined State Grid Smart Grid Research Institute, Beijing, China, as a Manager of HVDC Department. He is currently an Academician with the Chinese Academy of Engineering.

Zhiyuan He received the B.Eng. degree in Electrical Engineering from Sichuan University, Chengdu, China, in 2000, and M.Eng. degree and Ph.D. degrees in Electrical Engineering from China Electric Power Research Institute (CEPRI), Beijing, China, in 2003 and 2006, respectively. In 2006, he joined CEPRI, where he led the voltage sourced converter based high-voltage DC (VSC-HVDC) transmission system group. In the past ten years, he has accomplished theoretical study in high-power electronics technology for reliable operation of large interconnected power grids, relocatable DC de-ice systems, DC circuit breakers, and VSC-HVDC transmission, including the first VSCHVDC project commissioning in 2011 in China and 320 kV/1000 MW voltage sourced converter. He was a member of CIGRE B4 Working Group 48, and conducted research on components testing of VSC system for HVDC applications from 2006 to 2009. He has been a member of IEC SC22F WG19, MT22, and WG24 since 2009.

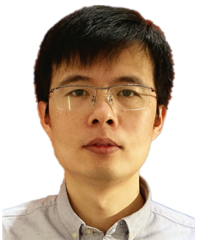

Zhiguang Lin received the B.Eng. and M.Eng. degrees in Electrical Engineering from North China Electric Power University, Baoding, China, in 2007 and 2010, respectively. Since 2010, he has been engaged in the research and engineering application of key technologies for renewable sources DC grid connection technology and equipment, ultra-HVDC/VSC-HVDC transmission control and protection.

Chong Gao received his B.S. degree from Yanshan University, Qinhuangdao, China, in 2005, and M.S. and Ph.D. degrees from China Electric Power Research Institute, Beijing, China, in 2008 and in 2017, respectively. He is currently a Professor-scale Senior Engineer with China Electric Power Research Institute. His main research interests include HVDC transmission, DC breakers, and DC grids.

Zixuan Zheng received B.S. and Ph.D. degrees in Electrical Engineering from Sichuan University, Chengdu, China, in 2012 and 2017, respectively. He is currently an Associate Professor with the College of Electrical Engineering, Sichuan University. His research interests include power quality, operation, and control of distributed energy resources.